

NEAR-FIELD OR FAR-FIELD FULL-WAVE GROUND PENETRATING RADAR MODELING AS A FUNCTION OF THE ANTENNA HEIGHT ABOVE A PLANAR LAYERED MEDIUM

Anh Phuong Tran^{1, *}, Frédéric André¹, Christophe Craeye², and Sébastien Lambot¹

¹Earth and Life Institute, Université catholique de Louvain, Croix du Sud, Box L7.05.02, Louvain-la-Neuve 1348, Belgium

²Institute of Information and Communication Technologies, Electronics and Applied Mathematics, Université catholique de Louvain, Place du Levant, Box L5.04.04, Louvain-la-Neuve 1348, Belgium

Abstract—The selection of a near-field or far-field ground-penetrating radar (GPR) model is an important question for an accurate but computationally effective characterization of medium electrical properties using full-wave inverse modeling. In this study, we determined an antenna height threshold for the near-field and far-field full-wave GPR models by analyzing the variation of the spatial derivatives of the Green's function over the antenna aperture. The obtained results show that the ratio of this threshold to the maximum dimension of the antenna aperture is approximately equal to 1.2. Subsequently, we validated the finding threshold through numerical and laboratory experiments using a homemade 1–3 GHz Vivaldi antenna with an aperture of 24 cm. For the numerical experiments, we compared the synthetic GPR data generated from several scenarios of layered medium using both near-field and far-field antenna models. The results showed that above the antenna height threshold, the near-field and far-field GPR data perfectly agree. For the laboratory experiments, we conducted GPR measurements at different antenna heights above a water layer. The near-field model performed better for antenna heights smaller than the threshold value (≈ 29 cm), while both models provided similar results for larger heights. The results obtained by this study provides valuable insights to specify the antenna height threshold above which the far-field model can be used for a given antenna.

Received 31 May 2013, Accepted 20 July 2013, Scheduled 26 July 2013

* Corresponding author: Anh Phuong Tran (phuong.tran@uclouvain.be).

1. INTRODUCTION

Over the last decades, ground-penetrating radar (GPR) has become an advanced non-destructive technique that is widely used in geoscience [14], archeology [11] and civil engineering [2, 12]. However, most of the existing techniques rely on strong simplifications concerning the wave propagation and antenna mutual coupling, which inherently limits the GPR effectiveness. Recently, with developments in computational technology, efforts have been made to model the antenna by numerical methods, e.g., finite difference time domain (FDTD) [1, 4], or method of moments (MoM) [5]. Yet, simultaneous modeling of the antennas and medium is still a challenge for these methods due to the different spatial resolution requirements of the two domains. It is also difficult to apply these methods in inverse modeling frameworks for the fact that they require a significant computation time.

For decreasing computation time, other authors attempted to find analytical solutions of Maxwell's equations by using several specific assumptions. For example, Gentili and Spagnolini [6] modeled a horn antenna at some distance over a three-dimensional (3-D) layered medium using an array of frequency independent source dipoles and a feeding line characteristic impedance. However, the interactions between antenna and medium were not considered in this model. Lambot et al. [10] developed a far-field antenna model to characterize planar layered media. The model accounts for the antenna effects through global transmission/reflection coefficients. The wave propagation in planar layered media is simulated using 3-D Green's function. Nevertheless, the model requires the antenna to be situated far enough from the medium to satisfy the far-field assumption. Lambot and André [9] generalized the far-field model so that it also applies to near-field conditions while still resorting to an analytical, closed-form solution of Maxwell's equations. The model was successfully validated in laboratory conditions. Comparison between this model and a FDTD-based model (GprMax, Giannopoulos [7]) was recently evaluated by Tran et al. [16]. Using this model, the antenna can operate nearer the dielectric medium, which reduces the emitting and back scattering radiuses. As a result, there is more information about medium contained in the GPR data, and therefore, the medium electrical properties can be better obtained. Moreover, the smaller footprint of the antenna in the near-field region makes the assumption of local homogeneity under the antenna footprint more valid.

Although the near-field GPR model provides more accurate estimations, the far-field one is more effective in terms of computation

time. However, it is not clear to which extent of the antenna height, the far-field GPR model holds. As a result, it is necessary to find an antenna height threshold for the selection of the GPR model depending on the antenna location. In this study, we theoretically estimate the antenna height threshold by analyzing the partial derivatives of the Green's function over the antenna aperture. Then, this threshold is validated by comparing the near- and far-field GPR models using both numerical and laboratory experiments.

2. THEORY

2.1. Green' Function

The propagation of electromagnetic waves in planar layered media can be simulated by the Green's functions, which are solutions of Maxwell's equations. In our case, the Green's functions are defined as the scattered x -directed electric field at the field point for a unit-strength x -directed electric source [10, 13]. In the spectral domain, the Green's function at the source point is written as below:

$$\tilde{G}_{..} = \left[\cos^2(k_\theta) \left(\frac{\Gamma_0 R_0^{\text{TM}}}{2\eta_0} + \frac{\zeta_0 R_0^{\text{TE}}}{2\Gamma_0} \right) - \frac{\zeta_0 R_0^{\text{TE}}}{2\Gamma_0} \right] \exp(-2\Gamma_0 h_0) \quad (1)$$

in which $G_{..}$ is the Green's function with dots (..) referring the field and the source points, respectively. R_0^{TM} and R_0^{TE} are the transverse magnetic (TM) and electric (TE) global reflection coefficients at the free-space interface accounting for all reflections from the N -layered medium. These coefficients are determined by using an upward recursive scheme as below:

$$R_n^{\text{TE}} = \frac{r_n^{\text{TE}} + R_{n+1}^{\text{TE}} \exp(-2\Gamma_2 h_{n+1})}{1 + r_n^{\text{TE}} R_{n+1}^{\text{TE}} \exp(-2\Gamma_{n+1} h_{n+1})} \quad (2)$$

$$R_n^{\text{TM}} = \frac{r_n^{\text{TM}} + R_{n+1}^{\text{TM}} \exp(-2\Gamma_{n+1} h_{n+1})}{1 + r_n^{\text{TM}} R_{n+1}^{\text{TM}} \exp(-2\Gamma_{n+1} h_{n+1})} \quad (3)$$

$$r_n^{\text{TE}} = \frac{\mu_{n+1}\Gamma_n - \mu_n\Gamma_{n+1}}{\mu_{n+1}\Gamma_1 + \mu_1\Gamma_{n+1}} \quad (4)$$

$$r_n^{\text{TM}} = \frac{\eta_{n+1}\Gamma_n - \eta_n\Gamma_{n+1}}{\eta_{n+1}\Gamma_n + \eta_n\Gamma_{n+1}} \quad (5)$$

where subscript n ($n = 0, \dots, N - 1$) denotes the index of the n th interface increasing from the top to bottom layer, in which $n = 0$ represents the upper half-space (free-space) interface; r_n^{TM} and r_n^{TE} are the TM- and TE-mode local reflection coefficients of the n th interface; h_n is the layer thickness with h_0 indicating the distance between the

source/receiver points and the first medium interface; Γ_n is the vertical wavenumber defined as $\Gamma_n = \sqrt{k_\rho^2 + \zeta_n \eta_n}$, whilst $\zeta_n = j\omega\mu_n$ and $\eta_n = \sigma_n + j\omega\varepsilon_n$ with μ_n , ε_n and σ_n are the dielectric permittivity, magnetic permeability and electrical conductivity, respectively. For the upper half-space, we have $\Gamma_0 = \sqrt{k_\rho^2 - (\frac{\omega}{c})^2}$ with c being the free-space wave velocity.

The upward recursive scheme begins to calculate the TM and TE global reflection coefficients at the interface $(N - 1)$ th with $R_{N-1}^{\text{TM}} = r_{N-1}^{\text{TM}}$ and $R_{N-1}^{\text{TE}} = r_{N-1}^{\text{TE}}$ for the fact that there is no reflection from the lower half-space.

The spatial-domain Green's functions are obtained from their spectral-domain counterpart using the inverse Fourier transform:

$$G_{..} = \left(\frac{1}{2\pi}\right)^2 \int_0^{+\infty} \int_0^{2\pi} \exp[-j\rho \cos(\theta)k_\rho \cos(k_\theta) + \rho \sin(\theta)k_\rho \sin(k_\theta)] \tilde{G}_{..} k_\rho dk_\rho dk_\theta \quad (6)$$

By introducing the first kind Bessel functions $J_m(k_\rho\rho)$:

$$J_m(k_\rho\rho) = \frac{(-j)^{-m}}{2\pi} \int_0^{2\pi} \exp(-jk_\rho\rho \cos(\varphi)) \cos(m\varphi) d\varphi \quad (7)$$

the 2-dimensional integral (6) can be reduced to a 1-dimensional one as below:

$$G_{..} = \frac{1}{8\pi} \int_0^{+\infty} [J_0(k_\rho\rho)\tilde{g}_1 - J_2(k_\rho\rho) \cos(2\theta)\tilde{g}_2] \exp(-2\Gamma_0 h_0) k_\rho dk_\rho \quad (8)$$

where

$$\tilde{g}_1 = \frac{\Gamma_0 R_0^{\text{TM}}}{\eta_0} - \frac{\zeta_0 R_0^{\text{TE}}}{\Gamma_0} \quad (9)$$

and

$$\tilde{g}_2 = \frac{\Gamma_0 R_0^{\text{TM}}}{\eta_0} + \frac{\zeta_0 R_0^{\text{TE}}}{\Gamma_0} \quad (10)$$

in which m denotes the order of the Bessel functions; $\rho = \sqrt{x^2 + y^2}$ and $\theta = \arctan(\frac{y}{x})$ are, respectively, the distance and angle in the xy -plane between the field and source points; k_ρ and k_θ are the horizontal Fourier transformation counterparts of ρ and θ .

2.2. Partial Derivative of Green's Function with Respect to Antenna Spatial Variables

The relationship between the far-field threshold and the antenna aperture size was investigated by analyzing the variations of the

backscattered field over the antenna aperture. Accordingly, we evaluated the partial derivatives of the Green’s function with respect to the antenna spatial variables, namely, ρ and θ . If these derivatives are equal to zero, the Green’s function is supposed to be constant everywhere in the region delineated by the antenna aperture and, therefore, the far-field assumption will be satisfied. From Equation (8), the derivatives are derived as:

$$\begin{aligned} \frac{\partial G..}{\partial \rho} &= \frac{1}{8\pi} \frac{\partial}{\partial \rho} \int_0^{+\infty} [J_0(k_\rho \rho) \tilde{g}_1 - J_2(k_\rho \rho) \cos(2\theta) \tilde{g}_2] \exp(-2\Gamma_0 h_0) k_\rho dk_\rho \\ &= \frac{1}{8\pi} \int_0^{+\infty} \left[\frac{\partial J_0(k_\rho \rho)}{\partial \rho} \tilde{g}_1 - \frac{\partial J_2(k_\rho \rho)}{\partial \rho} \cos(2\theta) \tilde{g}_2 \right] \exp(-2\Gamma_0 h_0) k_\rho dk_\rho \end{aligned} \quad (11)$$

$$\begin{aligned} \frac{\partial G..}{\partial \theta} &= \frac{1}{8\pi} \frac{\partial}{\partial \theta} \int_0^{+\infty} [J_0(k_\rho \rho) \tilde{g}_1 - J_2(k_\rho \rho) \cos(2\theta) \tilde{g}_2] \exp(-2\Gamma_0 h_0) k_\rho dk_\rho \\ &= \frac{1}{8\pi} \int_0^{+\infty} \left[J_0(k_\rho \rho) \tilde{g}_1 - J_2(k_\rho \rho) \frac{\partial \cos(2\theta)}{\partial \theta} \tilde{g}_2 \right] \exp(-2\Gamma_0 h_0) k_\rho dk_\rho \end{aligned} \quad (12)$$

It is worth noting that, in Formula (11), only the Bessel functions J_0 and J_2 depend on ρ , and in Formula (12), only the component $\cos(2\theta)$ depends on θ . After doing some rearrangements, we obtain:

$$\begin{aligned} \frac{\partial G..}{\partial \rho} &= \frac{1}{8\pi} \int_0^{+\infty} \left\{ -J_1(k_\rho \rho) \tilde{g}_1 - \frac{1}{2} \tilde{g}_2 \cos(2\theta) [J_1(k_\rho \rho) \right. \\ &\quad \left. + J_3(k_\rho \rho)] \right\} \exp(-2\Gamma_0 h_0) k_\rho^2 dk_\rho \end{aligned} \quad (13)$$

$$\frac{\partial G..}{\partial \theta} = \frac{1}{4\pi} \int_0^{+\infty} J_2(k_\rho \rho) \tilde{g}_2 \sin(2\theta) \exp(-2\Gamma_0 h_0) k_\rho dk_\rho \quad (14)$$

Formulas (13) and (14) indicate that the antenna height-dependent derivatives $\frac{\partial G..}{\partial \rho}$ and $\frac{\partial G..}{\partial \theta}$ are equal to zero only when the antenna height approaches the infinite, $h_0 \rightarrow +\infty$. This implies that the far-field condition cannot be perfectly satisfied with an finite value of h_0 . Consequently, we attempted to find an antenna height at which both of the above derivatives are relatively small as a practical threshold for the far-field modeling.

2.3. Near-field and Far-field Antenna Models

For validating the antenna height threshold, we compared the near- and far-field antenna models at different heights. The numerical and laboratory validations proved that the near-field antenna model works well in both near- and far-field conditions [9, 16]. Consequently, the antenna height threshold for the far-field modeling can be verified if the behaviors of the near- and far-field antenna models are approximately

identical at that threshold. The paragraphs below briefly present the two models:

Near-field antenna model: The near-field antenna model was proposed by Lambot and André [9] to accurately reproduce the radiated antenna field and capture the scattered field distribution in near- and far-field conditions. Resorting to the superposition principle approach, the model characterizes the antenna by an equivalent set of infinitesimal source/field points and frequency-dependent global reflection/transmission coefficients. With this characterization, the radiated and scattered fields of the antenna can be decomposed into plane waves and, therefore, the electromagnetic fields are calculated using 3-D Green's functions (Equation (8)). In the frequency domain, this antenna model is written as:

$$S = \frac{b}{a} = T_0 + T_s(\mathbf{I}_N - \mathbf{G}_0\mathbf{R}_s)^{-1}\mathbf{G}T_i \quad (15)$$

with

$$T_s = [T_{s,1} \quad T_{s,2} \quad \dots \quad T_{s,N}] \quad (16)$$

$$\mathbf{R}_s = \begin{bmatrix} R_{s,1} & 0 & \dots & 0 \\ 0 & R_{s,2} & \dots & 0 \\ \vdots & \vdots & \dots & \vdots \\ 0 & 0 & \dots & R_{s,N} \end{bmatrix} \quad (17)$$

$$T_i = [T_{i,1} \quad T_{i,2} \quad \dots \quad T_{i,N}]^T \quad (18)$$

$$\mathbf{G}_0 = \begin{bmatrix} G_{11}^0 & G_{12}^0 & \dots & G_{1N}^0 \\ G_{21}^0 & G_{22}^0 & \dots & G_{2N}^0 \\ \vdots & \vdots & \dots & \vdots \\ G_{N1}^0 & G_{N2}^0 & \dots & G_{NN}^0 \end{bmatrix} \quad (19)$$

and

$$\mathbf{G} = \begin{bmatrix} G_{11} & G_{12} & \dots & G_{1N} \\ G_{21} & G_{22} & \dots & G_{2N} \\ \vdots & \vdots & \dots & \vdots \\ G_{N1} & G_{N2} & \dots & G_{NN} \end{bmatrix} \quad (20)$$

where $S(\omega)$ is the ratio between the backscattered $b(\omega)$ and incident field $a(\omega)$ at the radar transmission line reference plane, with ω being the angular frequency; $T_0(\omega)$ denotes the global transmission or reflection coefficient of the antenna in free space; T_s is the global transmission coefficient vector for fields incident from the field points onto the radar reference plane; T_i is the global transmission coefficient vector for fields incident from the radar reference plane onto the point sources; and \mathbf{R}_s is the global reflection coefficient matrix for the field

incident from the layered medium onto the field points; \mathbf{I}_N is the N -order identity matrix; and superscript T denotes the transpose operator.

Far-field antenna model: When the far-field condition is satisfied, the scattered fields can be approximated by a plane wave. Hence, the antenna can be effectively characterized by an infinitesimal point source and receiver, which simplifies Equation (15) to the far-field model of Lambot et al. [10]:

$$S(\omega) = T_0 + \frac{T_{s,1}G_{11}T_{i,1}}{1 - G_{11}^0 R_{s,1}} \quad (21)$$

In order to apply the near- and far-field antenna models for quantitative reconstruction of a planar layered medium, the coefficients (T_0 , T_i , T_s and \mathbf{R}_s) need to be calibrated. We refer to Lambot and André [9] for the near-field calibration and Lambot et al. [10] for the far-field antenna calibration.

It is apparent that the far-field model is much effective in terms of computation time than the near-field one for the fact that it has a more simple radar equation and less Green's function evaluation. Indeed, we only need to calculate the Green's functions G_{11}^0 and G_{11} in the far-field model, while all $G_{..}^0$ and $G_{..}$ need to be evaluated in the near-field model. The larger the number of source/field points, the longer computation time we need. Therefore, the far-field model should be applied when the far-field condition is satisfied.

3. RESULTS AND DISCUSSION

3.1. Antenna Threshold for Far-field Antenna Modeling

Figure 1 shows the amplitude of the spatial complex derivatives of the Green's function versus the antenna height and frequency. Our evaluation was performed for a synthetic 2-layered medium. The upper and lower electrical properties of the medium were fixed to $\epsilon_{r1} = 4$, $\sigma_1 = 0.0063$ S/m and $\epsilon_{r2} = 9$, $\sigma_2 = 0.0296$ S/m, and their thicknesses were $h_1 = 12$ cm and $h_2 = 15$ cm, respectively.

We considered three antenna types: A homemade Vivaldi antenna, a linear polarized double-ridged horn antenna (BBHA 9120-F, Schwarzbeck Mess-Elektronik, Schönau, Germany) and a commercial bowtie antenna (400-MHz GSSI, Geophysical Survey Systems, Inc., <http://www.geophysical.com>). The Vivaldi antenna has an aperture of 24 cm and a height of 15 cm. It was operated in the frequency range 1–3.0 GHz with a frequency step of 8 MHz. The BBHA 9120-F antenna was operated in the frequency range 200–2000 MHz with a step of 6 MHz. Its aperture area is 68×95 cm². The model

5103–400 MHz GSSI antenna works in the time domain with a center frequency $f_c = 400$ MHz. The dipole spacing between the transmitter and receiver bowtie antennas is 16 cm and distance from the dipole to the edge of antenna housing is 6 cm. We selected the frequency range for this antenna from $f_c/2$ to $2f_c$ with a step 20 MHz. It is worth noting that the variable θ vanishes in the cases of the Vivaldi and BBHA 9120-F antennas as these two antennas act simultaneously as both transmitter and receiver.

In Figure 1, instead of using the antenna height, we used the ratio of the antenna height to the maximum dimension of the antenna aperture (h_0/D) to account for the dependence of the far-field antenna

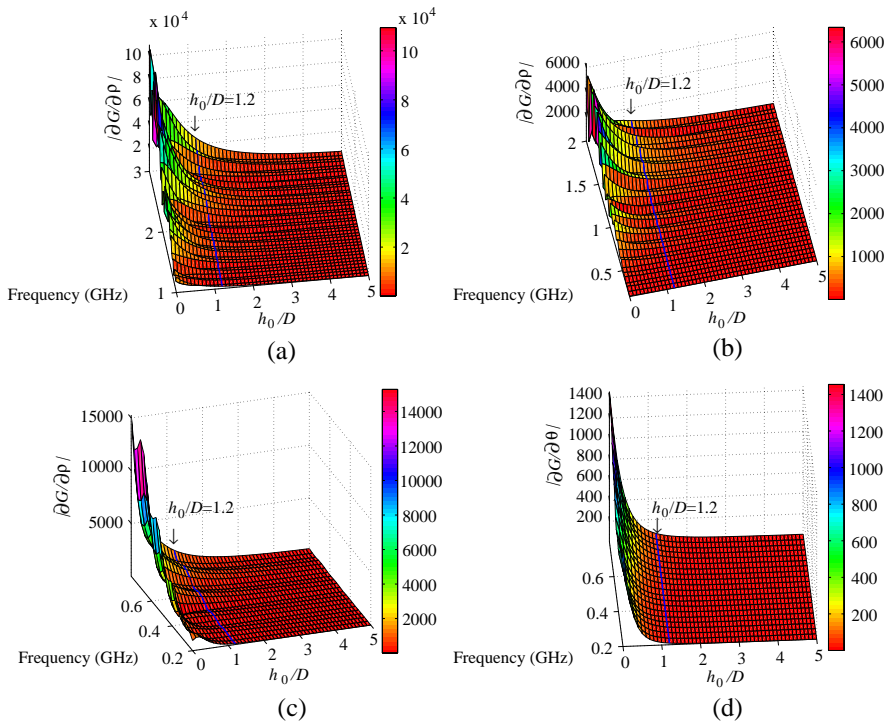


Figure 1. Derivatives of the Green's function with respect to the variables (a), (b), (c) ρ and (d) θ versus ratio of the antenna height to the maximum dimension of the antenna aperture (D) and frequency for (a) the Vivaldi, (b) BBHA 9120-F and (c), (d) 400-MHz GSSI antennas. The analysis used the 2-layered medium with $\epsilon_{r1} = 4$, $\sigma_1 = 0.0063$ S/m, $\epsilon_{r2} = 9$, $\sigma_2 = 0.0296$ S/m, $h_1 = 12$ cm and $h_2 = 15$ cm.

height threshold on the antenna aperture dimension. The figure shows that, for all antenna types, the amplitudes of the partial derivatives of the Green's functions are negatively proportional to the antenna height. They quickly reduce when the antenna height increases from 0 to around $1.2D$. After that, they slowly approach zero when the antenna height continues increasing. Figure 1 also shows that the amplitudes of the derivatives is higher for the higher frequency, implying that the Green's functions fluctuate more with increasing frequency. Yet, the effect of frequency on the derivatives is especially pronounced for the small antenna heights, while it appears to be insignificant when the antenna height is larger than about $1.2D$. Similar results were also obtained for the other scenarios of the medium. As a result, we may consider the antenna height $h_0 = 1.2D$ as a threshold for the near-field and far-field full-wave GPR models.

4. VALIDATION OF THE ANTENNA HEIGHT THRESHOLD

4.1. Numerical Experiments

In this section, we validated the antenna height threshold determined in the previous section by comparing the near- and far-field models using numerical experiments. We constructed a synthetic medium with 1 and 2 dielectric layers on an infinite perfect electrical conductor (PEC). For the 1-layered medium, the layer thickness is 15 cm and its relative dielectric permittivity and electrical conductivity are, respectively, $\varepsilon_r = 9$ and $\sigma = 0.0296$ S/m. In the case of the 2-layered medium, we used a layer thickness of 12 cm for the first layer and 15 cm for the second layer. With respect to the electrical properties of the medium, we considered two scenarios: scenario 1: $\varepsilon_{r1} = 4$, $\sigma_1 = 0.0063$ S/m, $\varepsilon_{r2} = 9$, $\sigma_2 = 0.0296$ S/m, and scenario 2: $\varepsilon_{r1} = 9$, $\sigma_1 = 0.0296$ S/m, $\varepsilon_{r2} = 4$, $\sigma_2 = 0.0063$ S/m.

We considered the Vivaldi antenna with the maximum aperture $D = 24$ cm, operating in a frequency range of 1–3.0 GHz and step of 8 MHz. The antenna characteristic global transmission/reflection coefficients were calibrated as presented in [9]. Numerical comparison between the two models was performed at different antenna heights ranging from 0.1 to $2D$. Figure 2 presents the GPR data generated by these models for the 1- and 2-layered medium scenarios. On the left panel, the magnitude and phase of the near- and far-field GPR data at the antenna height threshold ($h_0 = 1.2D$) are shown. The figure indicates that for all scenarios, the phases of the far-field antenna GPR data perfectly agree with the near-field ones. In terms of the magnitude values, there are negligible differences between the

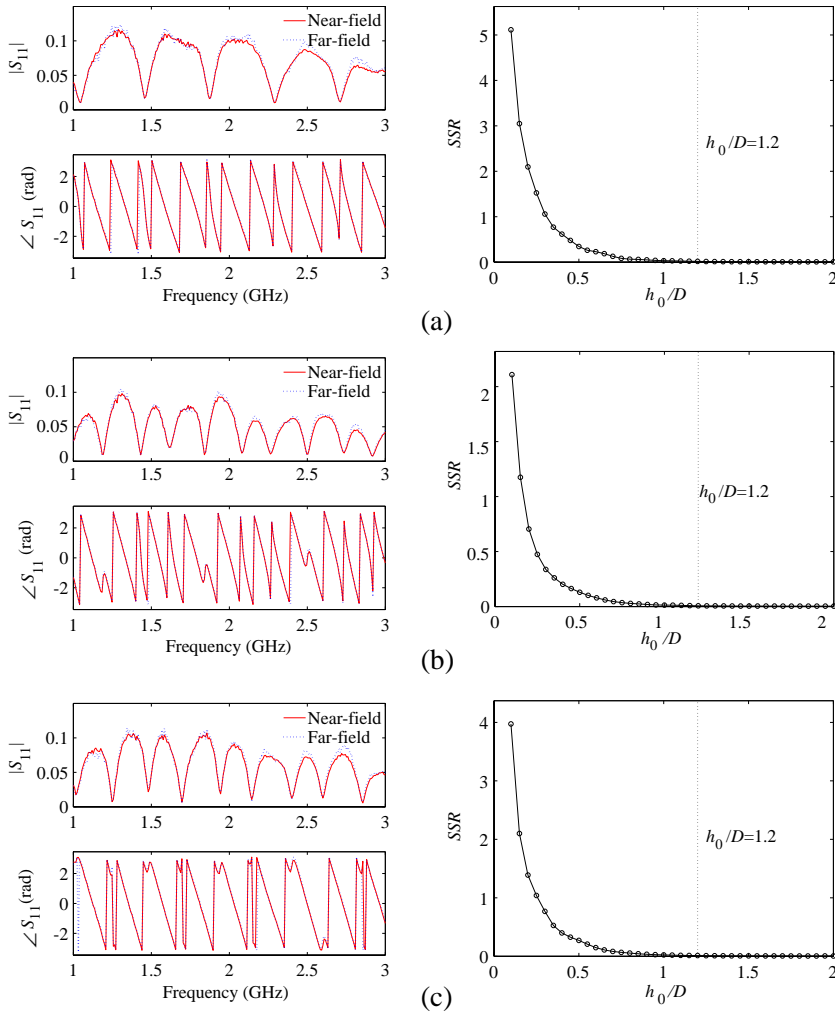


Figure 2. Comparison of the GPR data (S_{11}) generated by the near- and far-field antenna models under different scenario of dielectric medium. The left panel shows the magnitude and phase of the near- and far-field GPR data at the antenna height threshold for the far-field modeling ($h_0 = 1.2D$ with D being the maximum dimension of the antenna aperture). The right panel presents the sum of squared residuals (SSR) between near- and far-field GPR data as a function of the antenna height. (a) 1-layered medium: $\epsilon_r = 9$, $\sigma = 0.0296$ S/m. (b) 2-layered medium: $\epsilon_{r1} = 4$, $\sigma_1 = 0.0063$ S/m, $\epsilon_{r2} = 9$, $\sigma_2 = 0.0296$ S/m. (c) 2-layered medium: $\epsilon_{r1} = 9$, $\sigma_1 = 0.0296$ S/m, $\epsilon_{r2} = 4$, $\sigma_2 = 0.0063$ S/m.

two models, which is attributed to the errors of the global antenna characteristic transmission/reflection coefficients. The quantitative comparison between their synthetic GPR data was evaluated by the sum of squared residuals (SSR):

$$SSR = (S_{11}^{FF} - S_{11}^{NF})^T (S_{11}^{FF} - S_{11}^{NF}) \quad (22)$$

in which S_{11}^{NF} and S_{11}^{FF} are the complex near- and far-field GPR data vectors. The relationship between SSR and the antenna height is presented on the right panel of Figure 2. As expected, the discrepancy between the far- and near-field antenna models quickly decreases when the antenna height increases from $0.1D$ to $1.2D$. When the antenna height is larger $1.2D$, the difference is constant at around 0. This proves that the antenna height threshold $h_0 = 1.2D$ is suitable for the far-field modeling.

4.2. Laboratory Validation

For more realistic comparison of the near- and far-field models in terms of both GPR signals and parameter estimation, we carried out GPR measurements above a water layer with a thickness of 4.9 ± 0.1 cm on a copper plane. The GPR system works in the frequency domain and consists of a stepped-frequency continuous-wave vector network analyzer (VNA, ZVRE, Rohde Schwarz, Munich, Germany) and a homemade single Vivaldi antenna. The VNA and Vivaldi antenna were connected to each other by a 50Ω coaxial cable.

Measurements were conducted at 16 different antenna heights ranging from 0 cm to 70 cm. Temperature and electrical conductivity of water were 17.2°C and 0.0806 S/m , respectively. The frequency dependence of the water complex permittivity was described by the Debye model [3]. The relationship between the water temperature and the relaxation time was formulated by the Klein and Swift [8] equation, and between the temperature and the static permittivity by Stogryn's equation [15].

The antenna height and water thickness were considered as unknowns in this experiment. These variables were estimated at each antenna height by inverse modeling of GPR data using both near- and far-field models. The parameter space for the water thickness was $[2.5, 7.5]$ cm and extended from 50% to 150% of the measured values for the antenna height.

Figure 3 compares frequency-domain modeled GPR data obtained by the two models with measured ones at several heights from 0 to 29 cm. The near-field model reproduces very well the measured GPR data for all antenna heights. There are only small discrepancies in

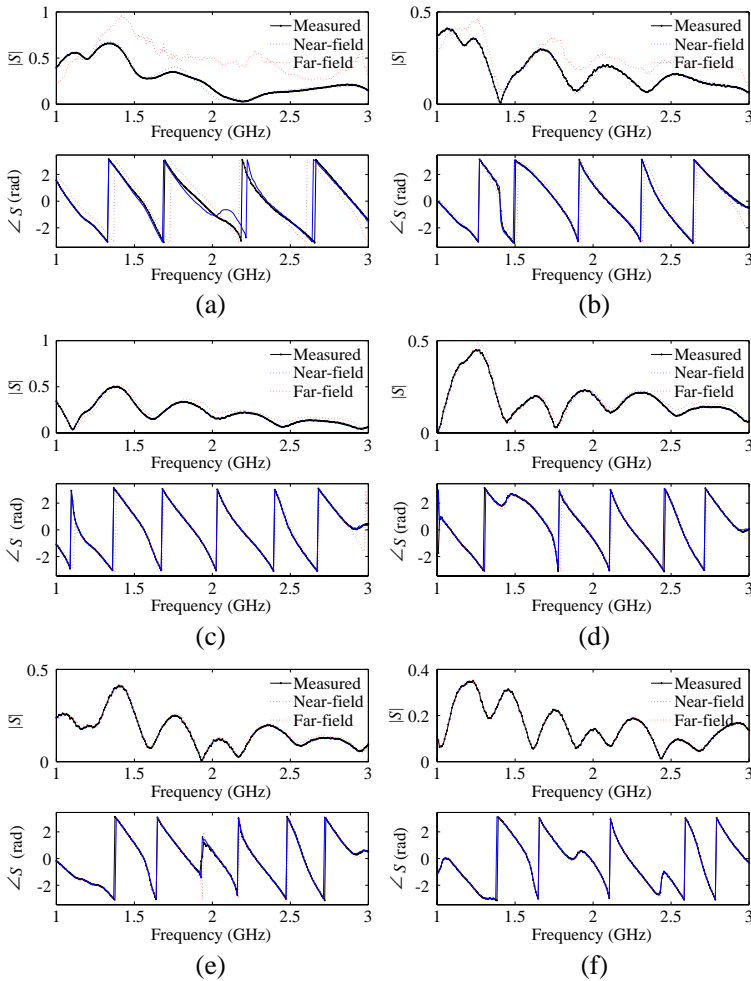


Figure 3. Comparison of the magnitude and phase of the near-field and far-field modeled GPR data with measured ones in the frequency domain domain at antenna heights of 0, 5, 10, 15, 20 and 29 cm. The experiments were performed in. (a) $h_0 = 0$ cm. (b) $h_0 = 5$ cm. (c) $h_0 = 10$ cm. (d) $h_0 = 15$ cm. (e) $h_0 = 20$ cm. (f) $h_0 = 29$ cm.

the range 1.7–2.2 GHz for an antenna height of 0 cm. In contrast, the agreement between far-field modeled and measured GPR data is not good as that observed for the near-field one. However, the difference between them considerably reduces as the antenna height increases. For antenna heights of 0 and 5 cm, the measurements are not well

reproduced by the far-field model. For antenna heights of 10 and 15 cm, although there are still some small gaps between far-field modeled and measured data, their difference significantly decreases. At 20 cm, the differences are negligible and at 29 cm ($1.2D$), we cannot differentiate the far-field GPR data from the near-field and measured ones.

Figure 4 shows the variation of SSR for the near- and far-field GPR models versus the antenna height. The figure excludes the SSR values corresponding with the antenna height equal to 0 cm because it is very large for the far-field model. When the antenna increases from 5 to 29 cm, while the SSR for the near-field model is constantly very small, that of the far-field model significantly decreases. When the antenna height is greater than 29 cm, the SSR of both models is identical and nearly equal to 0. This strengthens our findings that the antenna height $h_0 = 1.2D$ is a suitable threshold for the far-field modeling.

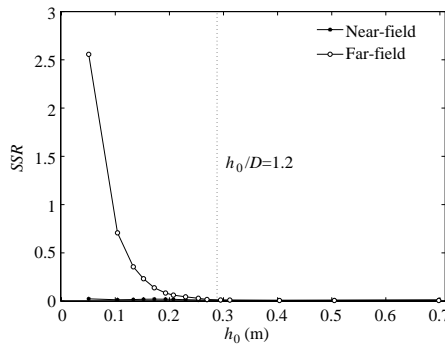


Figure 4. The RSS corresponding with the near- and far-field GPR models at different antenna heights.

Figure 5 compares the antenna height and water thickness estimated by the two models and their measured counterparts. The figure shows that the near-field model perfectly reproduces the antenna height and water thickness at all antenna heights. The high accuracy of the estimated parameters and very close agreement of modeled and measured GPR data prove the correctness of the near-field model and proper determination of its transmission/reflection coefficients. Therefore, this model can be used for characterization of the medium properties in both near- and far-field conditions. As for the far-field model, accurate results are also obtained for antenna heights greater than or equal to 5 cm. However, when the antenna contacts with the water surface, the estimated antenna height and water thickness are no longer reasonable. It is worth noting that although the SSR of the

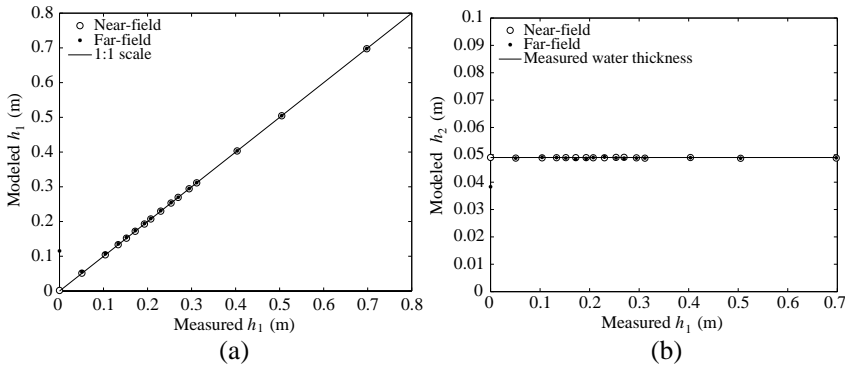


Figure 5. Comparison of measured and modeled (a) antenna height and (b) water thickness. The circle and asterisk markers describe the values estimated by near-field and far-field model, respectively.

far-field model increases significantly when the antenna moves from 29 cm down to 5 cm, the parameter estimation is still accurate. This might be explained by the small number of unknown parameters and high sensitivity of GPR data to these parameters.

5. CONCLUSION

We specified the antenna height threshold above which the far-field model can be effectively applied by evaluating the spatial variation of the Green's function over the antenna aperture. Accordingly, we calculated the partial derivatives of the Green's function with respect to the spatial polar coordinates (ρ, θ) , and analyzed their variations with different antenna heights and frequencies. Assuming that the Green's functions are approximately constant everywhere over the antenna aperture, and, therefore, equaling the amplitude of their spatial derivatives to zero, the antenna height threshold was found to be $h = 1.2D$ for all kinds of antennas.

We validated the above threshold both by numerical and laboratory experiments using a homemade 1–3 GHz Vivaldi antenna. For the numerical evaluation, we compared the synthetic GPR data generated by both of the near- and far-field antenna models above 1- and 2-layered scenarios with antenna heights ranging from 0.1 to $2D$. The obtained results indicate that above the antenna height threshold, the performance of the near- and far-field antenna models is similar, both in magnitude and phase.

For laboratory experiments, we compared the two models by

conducting GPR measurements from 0 to 70 cm above a water layer. The optimized results show that the near-field GPR model perfectly estimated the antenna height and water thickness at all antenna heights with very small difference between modeled and measured GPR data. The far-field model predicted well the unknown parameters for antenna heights beyond 5 cm ($\approx 0.2D$). Regarding the GPR data, the difference between far-field modeled and measured data increased rapidly as the antenna moved from 29 ($\approx 1.2D$) down to 0 cm. However, at antenna heights larger or equal to 29 cm, the far-field model data showed very good agreement with the near-field modeled and measured data.

ACKNOWLEDGMENT

This work was supported by the ARC project, the FNRS (Fonds National de la Recherche Scientifique, Belgium) and the Université catholique de Louvain (Belgium).

REFERENCES

1. Atteia, G. E. and K. F. A. Hussein, "Realistic model of dispersive soils using PLRC-FDTD with applications to GPR systems," *Progress In Electromagnetics Research B*, Vol. 26, 335–359, 2010.
2. Crocco, L., F. Soldovieri, T. Millington, and N. J. Cassidy, "Bistatic tomographic GPR imaging for incipient pipeline leakage evaluation," *Progress In Electromagnetics Research*, Vol. 101, 307–321, 2010.
3. Debye, P., *Polar Molecules*, Reinhold, New York, 1929.
4. Ernst, J. R., H. Maurer, A. G. Green, and K. Holliger, "Full-waveform inversion of crosshole radar data based on 2-D finite-difference time-domain solutions of Maxwell's equations," *IEEE Transactions on Geoscience and Remote Sensing*, Vol. 45, No. 9, 2807–2828, 2007.
5. Fernández Pantoja, M., A. G. Yarovoy, A. Rubio Bretones, and S. González García, "Time domain analysis of thin-wire antennas over lossy ground using the reflection-coefficient approximation," *Radio Science*, Vol. 44, No. 6, RS6009, 2009.
6. Gentili, G. G. and U. Spagnolini, "Electromagnetic inversion in monostatic ground penetrating radar: TEM horn calibration and application," *IEEE Transactions on Geoscience and Remote Sensing*, Vol. 38, No. 4, 1936–1946, 2000.
7. Giannopoulos, A., "Modelling ground penetrating radar by

- GPRMax,” *Construction and Building Materials*, Vol. 19, No. 10, 755–762, 2005.
8. Klein, L. A. and C. T. Swift, “An improved model for the dielectric constant of sea water at microwave frequencies,” *IEEE Transactions on Antennas and Propagation*, Vol. 25, No. 1, 104–111, 1977.
 9. Lambot, S. and F. André, “Full-wave modeling of near-field radar data for planar layered media reconstruction,” *IEEE Transactions on Geoscience and Remote Sensing*, 2013.
 10. Lambot, S., E. C. Slob, I. van den Bosch, B. Stockbroeckx, and M. Vanclooster, “Modeling of ground-penetrating radar for accurate characterization of subsurface electric properties,” *IEEE Transactions on Geoscience and Remote Sensing*, Vol. 42, 2555–2568, 2004.
 11. Papadopoulos, N., A. Sarris, M. Yi, and J. Kim, “Urban archaeological investigations using surface 3D ground penetrating radar and electrical resistivity tomography methods,” *Exploration Geophysics*, Vol. 40, No. 1, 56–68, 2009.
 12. Pettinelli, E., A. Di Matteo, E. Mattei, L. Crocco, F. Soldovieri, J. D. Redman, and A. P. Annan, “GPR response from buried pipes: Measurement on field site and tomographic reconstructions,” *IEEE Transactions on Geoscience and Remote Sensing*, Vol. 47, No. 8, 2639–2645, 2009.
 13. Slob, E. C. and J. Fokkema, “Coupling effects of two electric dipoles on an interface,” *Radio Science*, Vol. 37, No. 5, 1073, 2002.
 14. Steelman, C. M. and A. L. Endres, “Assessing vertical soil moisture dynamics using multi-frequency GPR common-midpoint soundings,” *Journal of Hydrology*, Vols. 436–437, 51–66, 2012.
 15. Stogryn, A., “The brightness temperature of a vertically structured medium,” *Radio Science*, Vol. 5, No. 12, 1397–1406, 1970.
 16. Tran, A. P., C. Warren, F. André, A. Giannopoulos, and S. Lambot, “Numerical evaluation of a full-wave antenna model for near-field applications,” *Near Surface Geophysics*, Vol. 11, No. 2, 155–165, 2013.